Access and sustainment of ELMy H-mode operation for ITER pre-fusion power operation plasmas using JINTRAC

PAPER • OPEN ACCESS

Access and sustainment of ELMy H-mode operation for ITER pre-fusion power operation plasmas using JINTRAC

To cite this article: E. Tholerus *et al* 2025 *Nucl. Fusion* **65** 036006

OPEN ACCESS
IOP Publishing | International Atomic Energy Agency
Nuclear Fusion
Nucl. Fusion **65** (2025) 036006 (16pp)
https://doi.org/10.1088/1741-4326/adaf3f

Access and sustainment of ELMy H-mode operation for ITER pre-fusion power operation plasmas using JINTRAC

E. Tholerus[1,*], L. Garzotti[1], V. Parail[1], Y. Baranov[1], X. Bonnin[2], G. Corrigan[1], F. Eriksson[1], D. Farina[3], L. Figini[3], D.M. Harting[4], S.H. Kim[2], F. Koechl[1], A. Loarte[2], E. Militello Asp[1], H. Nordman[5], S.D. Pinches[2], A.R. Polevoi[2] and P. Strand[5]

[1] UKAEA (United Kingdom Atomic Energy Authority), Culham Campus, Abingdon, Oxfordshire OX14 3DB, United Kingdom of Great Britain and Northern Ireland
[2] ITER Organization, Route de Vinon-sur-Verdon, CS 90 046, 13067 St. Paul Lez Durance Cedex, France
[3] Istituto per la Scienza e Tecnologia dei Plasmi, CNR, Milan, Italy
[4] Institut für Energie- und Klimaforschung IEK-4, FZJ, TEC, 52425 Jülich, Germany
[5] Association EURATOM-VR, Chalmers University of Technology, Göteborg, Sweden

E-mail: emmi.tholerus@ukaea.uk

Received 2 August 2024, revised 28 October 2024
Accepted for publication 28 January 2025
Published 10 February 2025

Abstract

In the initial stages of ITER operation, ELM mitigation systems need to be commissioned. This requires controlled flat-top operation in type-I ELMy H-mode regimes. Hydrogen or helium plasma discharges are used exclusively in these stages to ensure negligible production of neutrons from fusion reactions. With the expected higher L–H power threshold of hydrogen and helium plasmas compared to corresponding D and D/T plasmas, it is uncertain whether available auxiliary power systems are sufficient to operate in stable type-I ELMy H-mode. This has been investigated using integrated core and edge/SOL/divertor modelling with JINTRAC. Assuming that the L–H power threshold is well captured by the Martin08 scaling law, the presented simulations have found that 30 MW of ECRH power is likely required for the investigated hydrogen plasma scenarios, rather than the originally planned 20 MW in the 2016 Staged Approach ITER Baseline. However, past experiments have shown that a small helium fraction (∼10%) can considerably reduce the hydrogen plasma L–H power threshold. Assuming that these results extrapolate to ITER operation regimes, the 7.5 MA/2.65 T hydrogen plasma scenario is likely to access stable type-I ELMy H-mode operation also at 20 MW of ECRH.

* Author to whom any correspondence should be addressed.

Keywords: ITER, PFPO, scenario development, integrated modelling, JINTRAC

(Some figures may appear in colour only in the online journal)

1. Introduction

The ITER Pre-Fusion Power Operation (PFPO) is an important step in the ITER research plan [1] to demonstrate full technical capability of the ITER tokamak and to prepare for the main D and D–T campaigns. It is intended to demonstrate stable H-mode operation, as well as to commission several systems, such as auxiliary heating and current drive, fuelling, various diagnostics, edge localised mode (ELM) mitigation, and divertor heat flux control. PFPO will consist of two sub-phases. The first one, PFPO-1, will operate with at least 20 MW of electron cyclotron resonance heating (ECRH) and current drive (ECCD), and a selected set of diagnostics, fuelling and scenario control capabilities. The second sub-phase, PFPO-2, will operate with the full set of resources planned for baseline operation, including the ECRH capability of PFPO-1, 33 MW of hydrogen neutral beam injection (NBI) and 20 MW of ion cyclotron resonance frequency (ICRF) auxiliary heating and current drive[6]. All plasmas during PFPO will have hydrogen or helium as main ion species to ensure non-active operation.

This paper presents modelling of PFPO scenarios mainly intended for commissioning of the ELM mitigation systems. Unmitigated ELMs can severely damage the divertor, causing melting and cracking of the tungsten monoblock surfaces [3–6], especially during the high plasma current (15 MA) required for ITER baseline operation [6, 7]. One ELM mitigation technique that will be tested is resonant magnetic perturbations [1, 7, 8]. These are generated by a set of 27 in-vessel control coils, which can be used either to trigger smaller and more frequent ELMs or to fully or partially suppress the ELMs [7]. Artificially increasing the ELM frequency reduces the ELM energy fluence, with the ELM energy content ΔW_{ELM} being inversely proportional to the ELM frequency at constant P_{sep} [7]. Since the control coils will first be installed prior to PFPO-2 [1], alternative ELM mitigation techniques will be tested during PFPO-1, such as pellet pacing [9, 10] and vertical plasma oscillations [11, 12], which are also methods for artificially increasing the ELM frequency.

For successful commissioning of the ELM mitigation systems, operation in stable type-I ELMy H-mode is required. The presented scenarios are 5 MA/1.8 T and 7.5 MA/2.65 T, both operating with hydrogen as main ion species. Whether 20 MW ECRH is sufficient for stable ELMy H-mode operation or an additional 10 MW ECRH is required will be investigated. Methods for lowering the L–H power threshold will also be considered. The presented modelling only studies flat-top stages of the scenarios, starting from L-mode and setting up the density and auxiliary power required for triggering an L–H transition. The H-mode is sustained until the edge ballooning parameter α stabilises, which is then compared against the expected critical level for type-I ELM destabilisation, α_{crit}.

All simulations are performed with integrated core, edge, scrape-off layer and divertor modelling using JINTRAC [13], developed by EUROfusion. JINTRAC is unique in this capability, and it has been used for analysis of experiments in the past where interplay between core and edge/divertor physics is of importance [14, 15]. The two primary components of JINTRAC, JETTO (integrated core plasma model) and EDGE2D/EIRENE (scrape-off layer, private region, divertor, and wall model), have been well validated against experiments, see e.g. [16–18] (JETTO) and [19–21] (EDGE2D/EIRENE). Several core-only modelling efforts have been done in the past to assess the performance of PFPO plasmas [22–26]. In particular, one of these studies, [22], assessed type-I ELMy H-mode access for ITER 7.5 MA/2.65 T scenarios with both hydrogen, helium and deuterium plasmas using ASTRA [27]. The modelling, which included 20 MW of ECRH and 33 MW of NBI, demonstrated type-I ELMy H-mode access with helium and deuterium plasmas, with the hydrogen plasma scenario only reaching marginal H-mode access. The presented work expands this analysis by including (a) integrated modelling of both core, edge, scrape-off layer and divertor, (b) scenarios with an additional 10 MW of ECRH, (c) potential lowering of the L–H power threshold by the presence of a helium fraction (see details in section 2.3), and (d) similar studies of the 5 MA/1.8 T hydrogen plasma scenario.

2. Modelling assumptions

2.1. Integrated modelling structure

JINTRAC [13] is an integrated tokamak plasma model for simulation of the whole plasma, including core, pedestal, scrape-off layer (SOL), and private region (PR). It includes models for heating and current drive, self-consistent equilibrium calculation, transport (neoclassical and anomalous), fuelling (gas puffing and pellet injection), pumping, sputtering, atomic physics, sawteeth and ELMs. The two main components of JINTRAC are JETTO [28] and EDGE2D/EIRENE [29–31]. JETTO is a 1.5-dimensional core plasma model that simulates the plasma inside the last closed flux surface, whereas EDGE2D is a 2D SOL/PR Braginskii fluid model, and EIRENE simulates neutrals in the SOL/PR, including models for gas puffing, pumping, sputtering and recycling. EDGE2D/EIRENE is generally more computationally

[6] Following significant delays of the ITER experimental programme, an updated research plan is being formulated at the time of writing this paper (preliminary studies in support of the new research plan have been reported [2]). The updated research plan will likely impact the selection of scenarios during PFPO, the available auxiliary heating systems in different stages of ITER operation, and the wall material composition. All work presented here is based on the assumptions of the 2018 research plan [1].

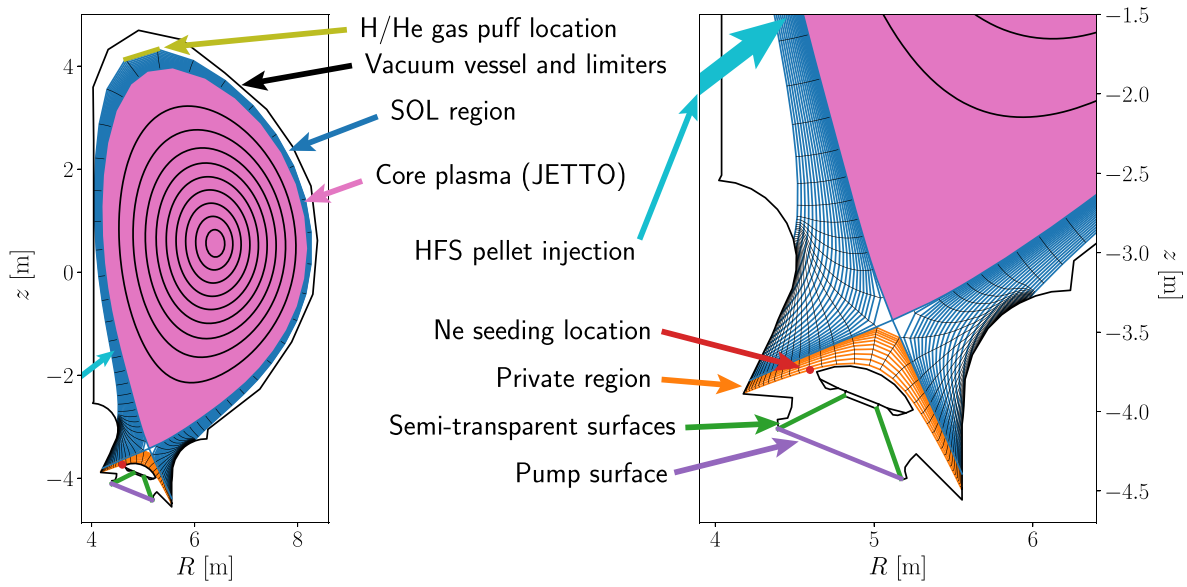

Figure 1. 2D geometric set-up for the presented JINTRAC simulations.

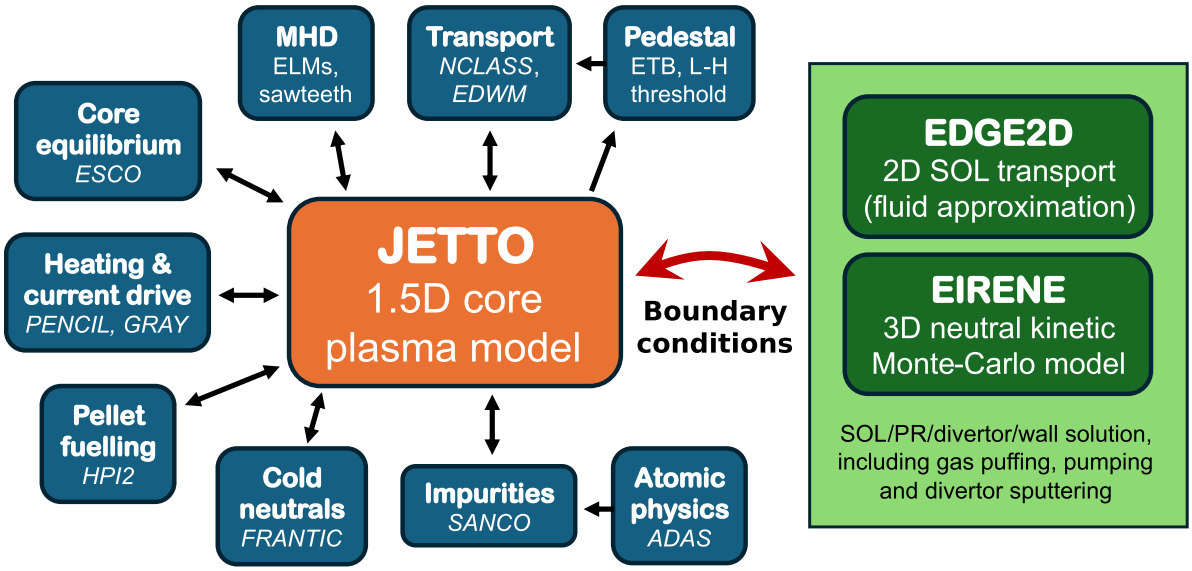

Figure 2. Block diagram of the JINTRAC integrated modelling structure. Arrows represent where data is passed between modules. In italics are different codes/databases integrated with JINTRAC, whereas models for e.g. magnetohydrodynamics (MHD), edge transport barrier (ETB) and L–H power threshold are intrinsic to JETTO.

demanding than JETTO for a given interval of plasma time. For numerical efficiency, JINTRAC typically utilises a partial coupling scheme between the codes, where JETTO and EDGE2D/EIRENE are fully coupled only during short intervals. In between the coupled phases, JETTO runs stand-alone for a selected interval (usually 2–20 times the coupled time interval). Fluxes are then rescaled at the EDGE2D/EIRENE boundary to compensate for the inactive time interval.

Figure 1 presents the geometric assumptions of the modelling, including first wall and divertor, fuelling and pumping surface locations. The EDGE2D grid, shown in blue and orange in the figure, is fixed, effectively fixing the geometry of the separatrix. Figure 2 shows an overview of the different components of JINTRAC, with arrows representing direct communication between modules. Boundary conditions between JETTO and EDGE2D/EIRENE are applied at the last closed flux surface. The following subsections describe how each component of JINTRAC is set-up in more detail, and which data that is communicated between them.

2.2. Heating and current drive

The 7.5 MA/2.65 T hydrogen plasma scenario is planned for PFPO-2, and is heated by a combination of ECRH and NBI. The 5 MA/1.8 T scenario is part of PFPO-1, and consequently does not include heating by NBI. Neither of the presented cases include heating by ICRF or lower hybrid (LH) waves. Heating by conventional ICRF schemes is not efficient

for the 7.5 MA/2.65 T hydrogen scenario [1, 32], whereas the 5 MA/1.8 T first H-mode scenario in the PFPO-1 phase has no installed ICRF power. However, there is a possibility that efficient heating based on three-ion schemes exists for the hydrogen scenarios with He-3 and He-4 minorities at 8.8 MA/3.13 T [33, 34]. As for LH heating and current drive, the launched wave spectra have a negative parasitic lobe that drives a counter-current near the edge, reducing the current drive efficiency to values below NBI current drive for ITER [35]. In addition, with the LH absorption primarily being in the edge plasma, the internal inductance is reduced, narrowing the operational space for MHD stability for ITER [36]. Two different ECRH power schemes are considered. The first scheme is 20 MW using the present baseline design of the ITER ECRH systems. In the second scheme, 10 MW of ECRH power is added to the baseline, assuming an upgrade of the ITER heating systems that is being assessed [1].

ECRH/ECCD is modelled predictively using the GRAY model [37]. The equatorial EC launchers operate in O-mode in the 7.5 MA/2.65 T scenarios, which gives less parasitic absorption and more efficient ECCD compared to X-mode operation during H-mode confinement, and X-mode in the 5 MA/1.8 T scenario. Some of the presented cases use the upper launcher for the suggested 10 MW ECRH upgrade, which operates in X-mode in scenarios where it is active. NBI heating and current drive is modelled with PENCIL [38], operating at full power (16.5 MW on each of the two negative ion source injectors), injecting hydrogen at ∼870 keV.

The bootstrap current is evaluated from neoclassical theory with NCLASS [39]. The total plasma current is set as a boundary condition in the simulations, with the inductive current and the corresponding loop voltage being adapted such that it completes the bootstrap and auxiliary currents to reach the set target value. With only flat-top stages being modelled, the total current is set to a constant level of either 5 MA or 7.5 MA depending on the scenario. The self-consistent handling of inductive current drive profiles and loop voltage together with current diffusion is described in [28].

2.3. L–H transition

The assumed L–H power threshold scaling law is based on Martin08 [40], with a correction $P_{\mathrm{L-H}} = P_{\mathrm{L-H,Martin08}} \times (2/A_{\mathrm{eff}})$ for hydrogenic plasmas [41]:

$$P_{\mathrm{L-H}} = 0.0488 \langle n_{\mathrm{e},20} \rangle_{\mathrm{line}}^{0.717} B_{\mathrm{tor}}^{0.803} S^{0.941} \left(2/A_{\mathrm{eff}}\right), \qquad (1)$$

where line-averaged electron density $\langle n_{\mathrm{e},20} \rangle_{\mathrm{line}}$ has the unit of $10^{20}\,\mathrm{m}^{-3}$, the toroidal magnetic field B_{tor} is in T, the cross sectional area of the last closed flux surface S is in m^2, and

$$A_{\mathrm{eff}} = \frac{\langle n_{\mathrm{H}} + 2n_{\mathrm{D}} + 3n_{\mathrm{T}} \rangle}{n_{\mathrm{H}} + n_{\mathrm{D}} + n_{\mathrm{T}}}. \qquad (2)$$

Since no deuterium or tritium is present in any of the PFPO scenarios, the correction factor $2/A_{\mathrm{eff}} = 2$. The scaling law of equation (1) is expected to have a larger uncertainty at low density, when $\langle n_{\mathrm{e}} \rangle \lesssim n_{\mathrm{e,min}} \approx 0.4 n_{\mathrm{GW}}$ [42], corresponding to a density $\langle n_{\mathrm{e}} \rangle \approx 2.5 \times 10^{19}\,\mathrm{m}^{-3}$ for the 7.5 MA scenario, and $\langle n_{\mathrm{e}} \rangle \approx 1.6 \times 10^{19}\,\mathrm{m}^{-3}$ for the 5 MA scenario. The density domain $\langle n_{\mathrm{e}} \rangle \gtrsim n_{\mathrm{e,min}}$ where the L–H power threshold follows the above scaling law is commonly referred to as the high-density branch of the L–H transition.

JET experiments have shown that both $P_{\mathrm{L-H}}$ and $n_{\mathrm{e,min}}$ are sensitive to the detailed strike-point configuration [43]. It was observed that by moving the outer strike point outwards from the horizontal target (HT) to the vertical target (VT) plate, $n_{\mathrm{e,min}}/n_{\mathrm{GW}}$ was reduced from around 40% to around 30% when operating JET at 3.0 T and 2.5–2.75 MA. The VT configuration also indicated a stronger density scaling than the 0.717 exponent of the Martin08 scaling in the high-density branch. On the other hand, the HT configuration showed similar $P_{\mathrm{L-H}}$ scaling with respect to density as the Martin08 scaling, but a value roughly 25% lower than $P_{\mathrm{L-H,Martin08}}$. It was hypothesised that the mechanism behind the dependence of $P_{\mathrm{L-H}}$ with respect to strike-point configuration is different degree of turbulence suppression by $E \times B$ shear in the edge region. It is non-trivial to translate these dependencies to ITER scenarios due to differences in divertor geometry between JET and ITER. However, the JET results can give an indication of the order of magnitude differences in $P_{\mathrm{L-H}}$ and $n_{\mathrm{e,min}}$ with respect to strike point configuration. The specific values of $P_{\mathrm{L-H}}$ and $n_{\mathrm{e,min}}$ assumed in the presented ITER model have resulted from compromises between several aspects of their respective observed dependencies in past experiments, details of which is beyond the scope of this paper.

JET experiments [44] have suggested that adding a certain fraction of helium can reduce $P_{\mathrm{L-H}}$ of hydrogen plasmas. Therefore, we will also consider the cases with and without added helium, assuming a 15% reduction of $P_{\mathrm{L-H}}$ when $\langle n_{\mathrm{He}} \rangle \approx 0.1 \langle n_{\mathrm{e}} \rangle$. Above all, to facilitate the access to H-mode, the basic assumption for L–H power threshold is to operate at densities close to $n_{\mathrm{e,min}} \approx 0.4 n_{\mathrm{GW}}$, as $P_{\mathrm{L-H}} \sim \langle n_{\mathrm{e}} \rangle^{0.717}$ [40]. It should be noted that JET experiments on helium plasmas have shown that $n_{\mathrm{e,min}}$ can range between $0.4 n_{\mathrm{GW}}$ and $0.7 n_{\mathrm{GW}}$ depending on the strike-point configuration [45]. This observation would need further investigation to determine how it extrapolates to ITER plasmas and strike-point configurations. The results presented here assume a reduction of $P_{\mathrm{L-H}}$ by a helium minority at $\langle n_{\mathrm{e}} \rangle \gtrsim 0.4 n_{\mathrm{GW}} \approx 2.5 \times 10^{19}\,\mathrm{m}^{-3}$ (cases D and E, as presented below).

H-mode access is determined by comparing $P_{\mathrm{L-H}}$ against $P_{\mathrm{net}} = P_{\mathrm{ECRH}} + P_{\mathrm{NBI}} + P_{\mathrm{ohm}} - P_{\mathrm{rad}} - \langle \mathrm{d}W_{\mathrm{p}}/\mathrm{d}t \rangle$, where P_{rad} is the combined impurity radiation and bremsstrahlung from the core plasma (inside the last closed flux surface), and $\langle \mathrm{d}W_{\mathrm{p}}/\mathrm{d}t \rangle$ is the time derivative of the total stored energy W_{p}, averaged over a time window of 5–50 ms for numerical stability. During H-mode ($P_{\mathrm{net}} \geqslant P_{\mathrm{L-H}}$), the diffusivity of the transport barrier domain is continuously lowered according to

$$D_{s,\mathrm{ETB}} = D_{s,\mathrm{NCLASS}} + \left[\theta + k_{\mathrm{sup}} (1 - \theta)\right] D_{s,\mathrm{anom}}. \qquad (3)$$

Here, s is the ion species index, $D_{s,\mathrm{NCLASS}}$ is the neoclassical particle diffusivity, $D_{s,\mathrm{anom}}$ is the unsuppressed anomalous diffusivity in the transport barrier, $k_{\mathrm{sup}} = 1.0 \times 10^{-3}$ is a numerical suppression factor, and

$$\theta = \exp\left(-\frac{P_{\text{net}} - P_{\text{L-H}}}{P_{\text{L-H}}\Delta_{\text{L-H}}}\right), \tag{4}$$

where $0.05 \leqslant \Delta_{\text{L-H}} \leqslant 0.1$ is a factor that sets the rate at which the suppressed transport barrier is approached for $P_{\text{net}} \geqslant P_{\text{L-H}}$. Similarly, a transport barrier forms in the heat diffusivities, χ_{e} and χ_{i}. Both the anomalous particle and heat diffusivities includes a 10% Bohm correction for enhanced ETB transport (see details in section 2.5). When the edge ballooning parameter α exceeds α_{crit}, the ETB diffusivities are smoothly up-scaled on feedback against α to prevent it from growing far above α_{crit} (see details in section 2.6).

2.4. Fuelling and impurity seeding

Fuelling by hydrogen gas puffing alone is sufficient for low density plasmas ($\langle n_{\text{e}} \rangle \lesssim 2 \times 10^{19}\,\text{m}^{-3}$). However, at high gas fuelling rates there is a risk of detachment due to excessive cooling of the edge plasma. A detached plasma configuration is generally avoided in the presented simulations. Although detachment access can potentially reduce divertor heat loads, conventional detachment techniques might also reduce core plasma density control. For numerical efficiency, EDGE2D/EIRENE does not include the molecular reactions necessary to accurately model detachment. In order to reduce the risk of detachment access, some of the presented scenarios do hydrogen fuelling by a combination of gas puffing and pellet injection (cases D and E, summarised in section 2.7). The additional pellet injection also allows for access to higher densities, as will be demonstrated for case E. Pellet ablation and deposition is modelled with HPI2 [46].

In order to avoid unacceptable levels of NBI shine-through power in lower density regimes that can reduce the life expectancy of the NBI shield blocks, a neon minority can be introduced to the core plasma to increase the beam stopping cross section [47]. The required concentration of neon depends on the total density of the plasma, with higher densities requiring less neon for sufficient beam stopping. In these simulations, neon gas rates are adapted to reach stabilised total shine-though power below about 1.8 MW while avoiding full divertor detachment. The simulations also consider critical upper limits associated with excessive impurity radiation, for instance a reduction of the net power flux across the separatrix due to core radiation, limiting the possibility to sustain stable ELMy H-mode operation, or a fully detached plasma by excessive edge/SOL cooling. Neon is also more efficient than H and He at sputtering tungsten from the divertor, potentially adding significantly to the impurity radiation.

SANCO [48] is used for modelling impurity atomic physics in the core, including radiation and ionisation/recombination, and EIRENE is used in the SOL and private region. Helium and neon atomic data is based on [49], and tungsten data is based on [50], which both exist in the ADAS database[7]. Charge state bundling schemes have been used both for neon (5 charge state levels) and tungsten (6 charge state levels), rather than following all ionisation stages for these impurities, as this significantly reduces the computing power required for SANCO.

2.5. Transport

Core heat and particle transport for both the main plasma and impurity species are handled by NCLASS [39] (neoclassical transport) and EDWM [51] (anomalous transport). In EDWM, saturated wave modes and resulting transport coefficients are predicted from linear growth rates, frequencies and other plasma parameters using quasi-linear theory. Only ion scale turbulence is considered in EDWM, such as ion temperature gradient and trapped electron modes. The simulations consider corrections to turbulence from collisionality and $E \times B$ shear. Five modes are considered in the poloidal mode spectrum, namely $k_{\perp}\rho_{\text{H}} = \{0.15, 0.2, \sqrt{0.1}, 0.4, 0.5\}$, where $k_{\perp}$ is the poloidal wave number, and $\rho_{\text{H}} = c_{\text{s,H}}/\Omega_{\text{c,H}}$ is the hydrogen gyro-radius ($c_{\text{s,H}}$ is the thermal sound speed, and $\Omega_{\text{c,H}}$ is the hydrogen gyro-frequency). A Casati-filter [52] for rescaling of the flux contributions from each mode is applied, similar to what has been implemented in the quasi-linear transport model QuaLiKiz [53].

A Bohm semi-empirical anomalous heat diffusivity [54] has been added on top of the EDWM and NCLASS diffusivities with a correction factor of 0.1, i.e.

$$\chi_{\text{i/e}} = \chi_{\text{i/e,NCLASS}} + \chi_{\text{i/e,EDWM}} + 0.1\chi_{\text{i/e,Bohm}}. \tag{5}$$

Similarly, the particle diffusivities has a correction

$$D_s = D_{s,\text{NCLASS}} + D_{s,\text{EDWM}} + 0.1\xi\left(\rho_{\text{tor}}\right)\frac{\chi_{\text{e,Bohm}}\chi_{\text{i,Bohm}}}{\chi_{\text{e,Bohm}} + \chi_{\text{i,Bohm}}}, \tag{6}$$

where $\xi(\rho_{\text{tor}}) = 1.0 - 0.7\rho_{\text{tor}}$. The additional Bohm-terms are introduced to enhance transport in the edge/pedestal region, where EDWM frequently underestimates heat diffusivities. The specific Bohm correction factor of 0.1 and the linear weight function $\xi(\rho_{\text{tor}})$ on the particle diffusivities match simulations of JET experiments with EDWM + Bohm predictive transport. During H-mode confinement, the EDWM and Bohm terms are suppressed by a factor according to equation (3).

The particle diffusivity of ion species s in the scrape-off layer is determined from the computed diffusivity at the last closed flux surface $D_{s,\text{sep}}$ (including edge transport barrier in H-mode confinement). A diffusivity D_{bnd} is set at the EDGE2D boundary surface. The full diffusivity profile then follows

$$D_{s,\text{SOL}}\left(x\right) = \begin{cases} D_{\text{bnd}} + \left(D_{s,\text{sep}} - D_{\text{bnd}}\right)Y_{\text{SOL}}^{x/\Delta_{\text{SOL}}} & \text{for } D_{s,\text{sep}} \geqslant D_{\text{bnd}}, \\ D_{s,\text{ETB,SOL}}\left(x\right) & \text{for } D_{s,\text{sep}} < D_{\text{bnd}}, \end{cases} \tag{7}$$

$$D_{s,\text{ETB,SOL}}\left(x\right) = \begin{cases} D_{s,\text{sep}} & \text{for } x < \Delta_{\text{ETB}}, \\ D_{s,\text{tanh}}\left(x\right) & \text{for } \Delta_{\text{ETB}} \leqslant x < \Delta_{\text{ETB}} + \Delta_{\text{tanh}}, \\ D_{\text{bnd}} & \text{for } x \geqslant \Delta_{\text{ETB}} + \Delta_{\text{tanh}}, \end{cases} \tag{8}$$

$$D_{s,\text{tanh}}\left(x\right) = D_{s,\text{sep}} + \frac{D_{\text{bnd}} - D_{s,\text{sep}}}{2} \times \left[1 + \tanh\left(2\pi\left[\frac{2\left(x - \Delta_{\text{ETB}}\right)}{\Delta_{\text{tanh}}} - 1\right]\right)\right], \tag{9}$$

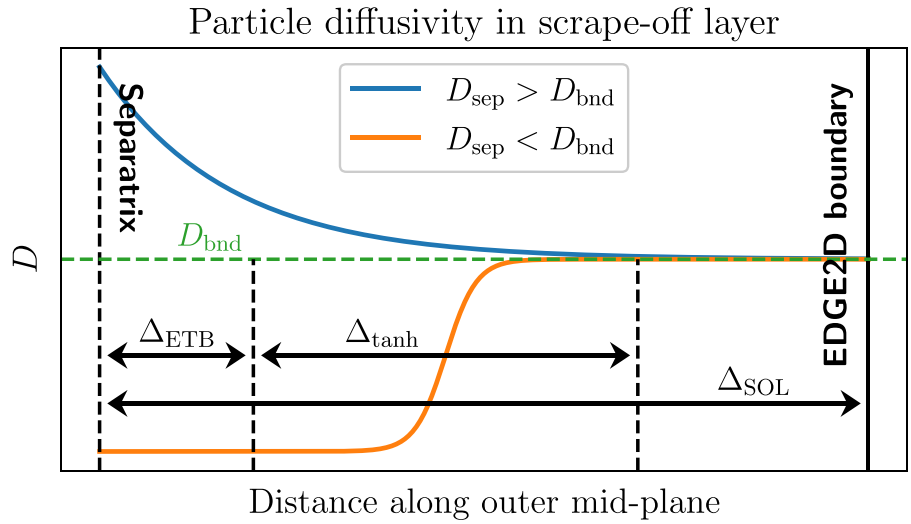

Figure 3. Particle diffusivity in the SOL for two different cases of $D_{s,sep}$ (diffusivity at the separatrix of ion species s, calculated by JETTO).

where x is the distance from the separatrix along the mid-plane. The model parameters are $D_{bnd} = 0.3 m^2\ s^{-1}$, $Y_{SOL} = 2.5 \times 10^{-3}$, $\Delta_{ETB} = 0.5$ cm, $\Delta_{tanh} = 0.3$ cm, and $\Delta_{SOL} = 7.81$ cm. The thermal diffusivity profiles are defined by the same model function (continuations of $\chi_{e,sep}$ and $\chi_{i,sep}$, respectively), with the same values of Y_{SOL}, Δ_{ETB}, Δ_{tanh} and Δ_{SOL} as for the particle diffusivity, but with $\chi_{e,bnd} = \chi_{i,bnd} = 1.0\,m^2\,s^{-1}$. Similarly, a smoothening is applied to diffusivities at the boundary between the ETB and the core (see details in [55]).

2.6. Equilibrium & MHD

The equilibrium was calculated from predicted pressure and current drive in the core plasma (inside the separatrix) by solving the Grad–Shafranov equation for a fixed separatrix geometry using ESCO [28]. The separatrix geometry was calculated for the 15 MA/5.3 T baseline scenario [56], using the free-boundary equilibrium solvers CORSICA [57] and DINA [58]. It is assumed that the same separatrix shape can be used for the flat-top cases studied in this paper, which all have the same I_p/B_{tor} ratio as the 15 MA/5.3 T scenario. A Kadomtsev model [59] has been used for sawtooth triggering and relaxation.

JETTO includes a continuous ELM model, which has been used with the assumption $\alpha \geqslant \alpha_{crit} = 1.8$ for triggering of type-I ELMs. Ideal MHD calculation of similar scenarios have predicted slightly higher values for α_{crit} between 2.0 and 2.5 [60]. The way that the continuous ELM model in JETTO gradually increases transport when $\alpha > \alpha_{crit}$ means that α saturates at a level slightly above α_{crit}. For this reason, a value $\alpha_{crit} = 1.8 < 2.0$ has been selected. H-mode operation with $\alpha < \alpha_{crit}$ corresponds more closely to an ELM-free or type-III ELM regime, with no up-scaling of the edge transport barrier. Since the primary purpose of the presented studies is to determine conditions for access to type-I ELMy H-mode regimes, the impact of discrete ELMs (mitigated or uncontrolled) on divertor and plasma facing components is beyond the scope of this paper (more detailed studies on these topics are presented in [7]). Divertor particle and power loads are only indirectly impacted by type-I ELMs via the up-scaling of the edge diffusivities in the continuous ELM model, which extend a given distance into the SOL as illustrated in figure 3.

2.7. Summary of scenarios

A total of 6 cases have been modelled with JINTRAC, labelled as follows:

- Case A: 5 MA/1.8 T hydrogen plasma with no added helium and 30 MW of ECRH.
- Case B: 7.5 MA/2.65 T H-plasma with no added helium, and 20 MW of ECRH + 33 MW of NBI.
- Case C.1: 7.5 MA/2.65 T H-plasma with no added helium, and 30 MW of ECRH + 33 MW of NBI.
- Case C.2: Repetition of part of the case C.1, but with a smaller amount of neon being gas puffed for assisting the beam stopping.
- Case D: 7.5 MA/2.65 T H-plasma with ∼10% added helium, and 20 MW of ECRH + 33 MW of NBI.
- Case E: 7.5 MA/2.65 T H-plasma with ∼10% added helium, and 30 MW of ECRH + 33 MW of NBI.

All of the presented JINTRAC simulations were running on Intel(R) Xeon(R) CPU E5-2665 0 @ 2.40 GHz processors on a single core. Depending on the numerical precision used for the core–edge coupled time stepping scheme, each second of plasma time took between 2 days and 2 weeks to simulate. The presented simulations only present the initial stages of flat-top operation, with less than 8 seconds of plasma seconds in each scenario. This is sufficient to demonstrate L–H transition and convergence of the edge ballooning parameter α.

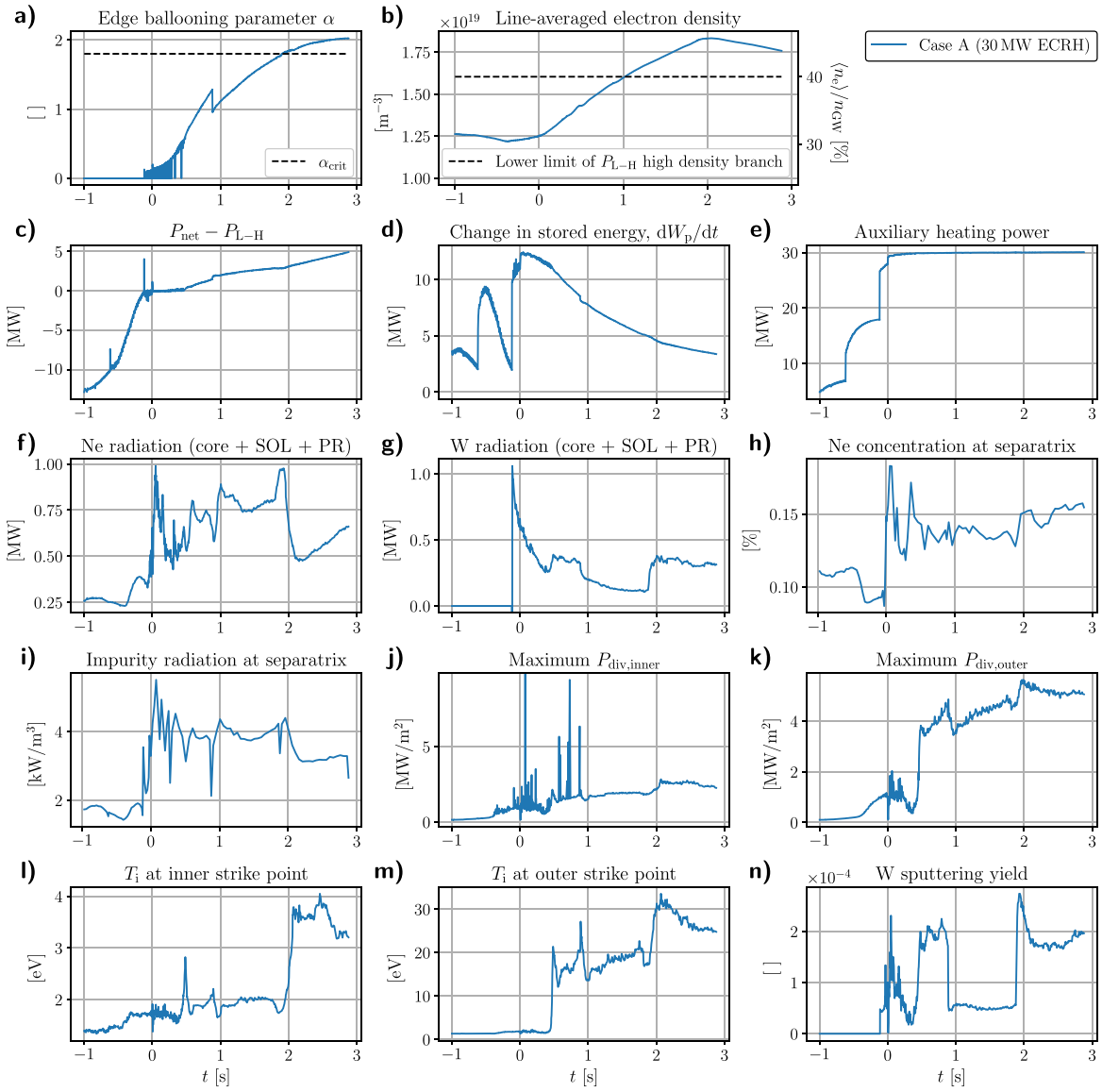

Figure 4. ITER 5 MA/1.8 T hydrogen plasma. The horizontal axis in each of the plots is time [s], offset such that $t = 0$ corresponds to the time of full auxiliary power injection. Auxiliary heating is done by ECRH only.

3. Results

3.1. 5 MA/1.8 T scenario

The 5 MA/1.8 T scenario is planned for the PFPO-1 stage of operation, where NBI is unavailable [24]. Consequently, auxiliary heating is done by microwave frequency only. Case A in figure 4 was run with 30 MW ECRH. As demonstrated in figure 4(*a*), the edge ballooning parameter exceeds α_{crit}. The net power difference above the L–H threshold is still increasing towards the end of the simulation, indicating that type-I ELMy H-mode can be maintained for long-pulse operation. In the early phases of H-mode operation, before $t \approx 1$ s, the line averaged electron density is below $n_{e,min}$. The Martin08 P_{L-H} scaling law has been assumed also in this regime, which is likely an underestimation of the power threshold. For this reason, the transition to H-mode might occur later in practice than what the modelling shows. As long as the plasma can be sufficiently fuelled to reach the high-density branch of P_{L-H}, the modelling assumptions do not change the conclusion that the scenario can operate in stable ELMy H-mode.

The results of the presented 30 MW case indicate that a corresponding 20 MW case would not be able to operate in H-mode. This can be understood from comparing figures 4(*c*) with 4(*d*). At the end of the simulation, P_{net} is about 4.9 MW above P_{L-H}. An additional margin of 3.4 MW (dW_p/dt at the end of the simulation in figure 4(*d*)) can be expected in steady-state conditions, where dW_p/d$t \to 0$, totalling to $P_{net} - P_{L-H} \approx 8.3$ MW. Dropping auxiliary power by 10 MW in these conditions would then place the net power about 1.7 MW below the power threshold. However, it should be noted that the density operates at a level above the lower limit of the high-density branch, as seen in figure 4(*b*). Assuming operation exactly at $\langle n_e \rangle = n_{e,min} \approx 0.4 n_{GW}$, equation (1) predicts a power threshold $P_{L-H} \approx 20.1$ MW. The estimated core

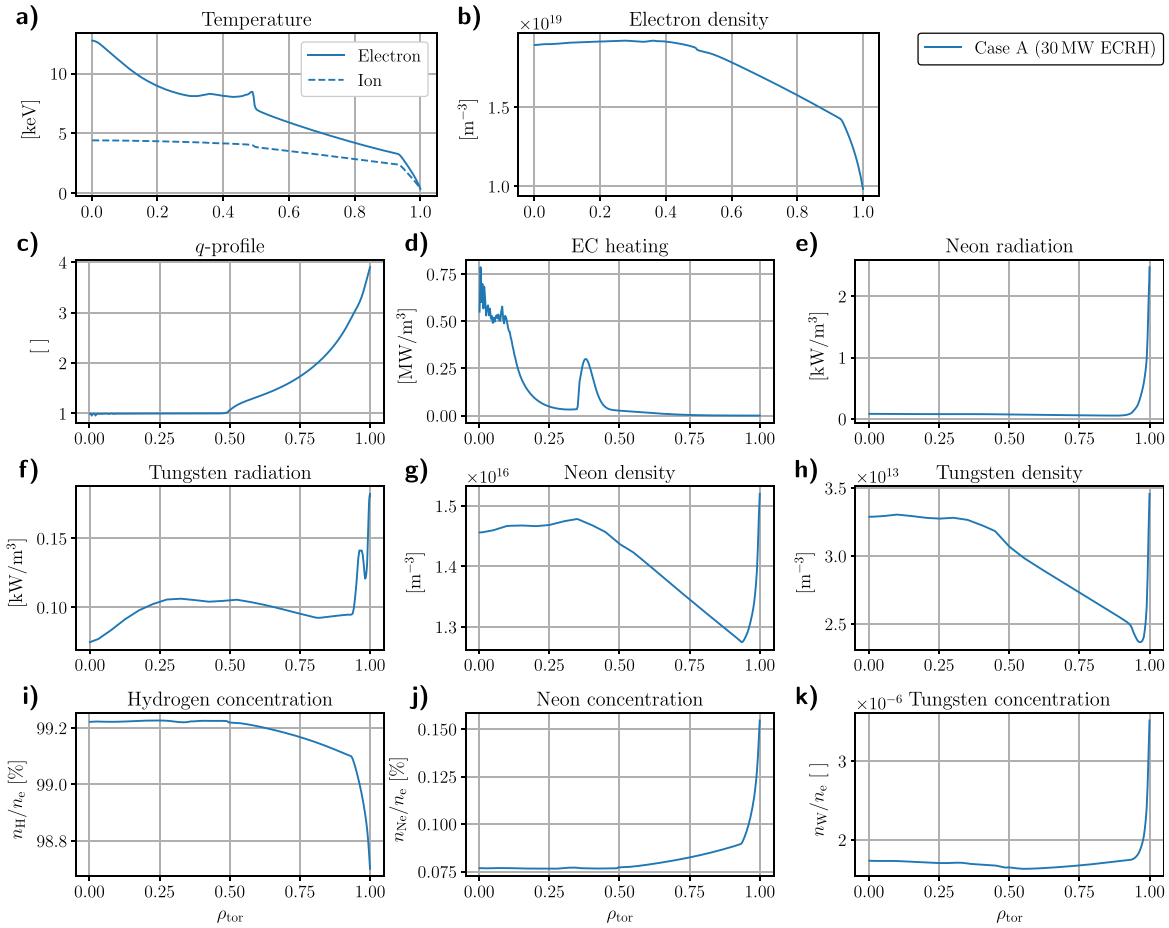

Figure 5. Core profile data for case A at the end time of the simulation ($t = 2.88$ s).

radiation losses exceed the ohmic heating by almost 0.3 MW. Subtracting this from 20 MW of auxiliary power results in a net power of 19.7 MW during steady-state conditions, which is 0.4 MW less than P_{L-H}.

The benefit of helium seeding has not yet been explored for this scenario. Assuming a 15% (i.e. about 3 MW) reduction of P_{L-H} by helium seeding, keeping the same assumptions about the ohmic heating and impurity radiation as demonstrated in the presented case in figure 4, would bring the net power about 2.6 MW above the power threshold during 20 MW ECRH operation. Comparing figures 4(*a*) and (*c*), this is very close to the power difference at which α exceeds α_{crit} in the demonstrated case. However, taking into account uncertainties in the underlying power threshold assumptions, it is not evident that an ELMy H-mode operational space exists in the helium seeded 5 MA/1.8 T hydrogen plasma scenario at 20 MW ECRH.

Since there is no NBI heating for this scenario, neon is not required for beam stopping. However, neon puffing is still used for suppressing the divertor power loads. As can be seen in figure 4(*h*), the neon concentration at the separatrix finishes around 0.15%, which is significantly lower than the corresponding concentration levels for the NBI scenarios (see figures 6(*k*) and 10(*k*)), which is of the order of a few percent. Reduced lifetime of the divertor would be expected for long-pulse operation with power loads above about 10 MW m^{-2} [1]. However, the divertor power loads never exceed 5 MW m^{-2}, besides single bursts on the inner divertor target plates during the initial stage of the H-mode, as seen in figures 4(*j*) and (*k*).

Tungsten sputtering from the divertor was not included during the L-mode phase of the simulation, as can be seen in figure 4(*g*). It was included at the start of the dithering phase, at $t = -0.12$ s. During the H-mode phase, there were two instances of rapid increase of the strike point ion temperature and the tungsten sputtering yield from the divertor, at $t \approx 0.45$ s and $t = 1.88$ s, as seen in figures 4(*l*)–(*n*). However, the associated tungsten radiation in the plasma volume remained at modest levels, below 400 kW, throughout most of the H-mode phase.

Figure 5 shows miscellaneous core 1D profile data for the 5 MA/1.8 T scenario at the end time of the simulations ($t = 2.88$ s). The additional 10 MW on the upper EC launcher gives no power absorption inside $\rho_{tor} = 0.35$, with a peak resonance around $\rho_{tor} = 0.38$, as seen in figure 5(*d*). The non-monotonic electron temperature profile of figure 5(*a*) is a result of both the off-axis ECRH and sawtooth crashes up to $\rho_{tor} \approx 0.5$ (domain with $q \approx 1$ in figure 5(*c*)). There is some degree of impurity accumulation, as seen in the peaked impurity density profiles of figures 5(*g*) and (*h*). However, core impurity concentrations are relatively low, with less than 0.1% of neon, and less than 2×10^{-6} of tungsten, as seen in figures 5(*j*) and

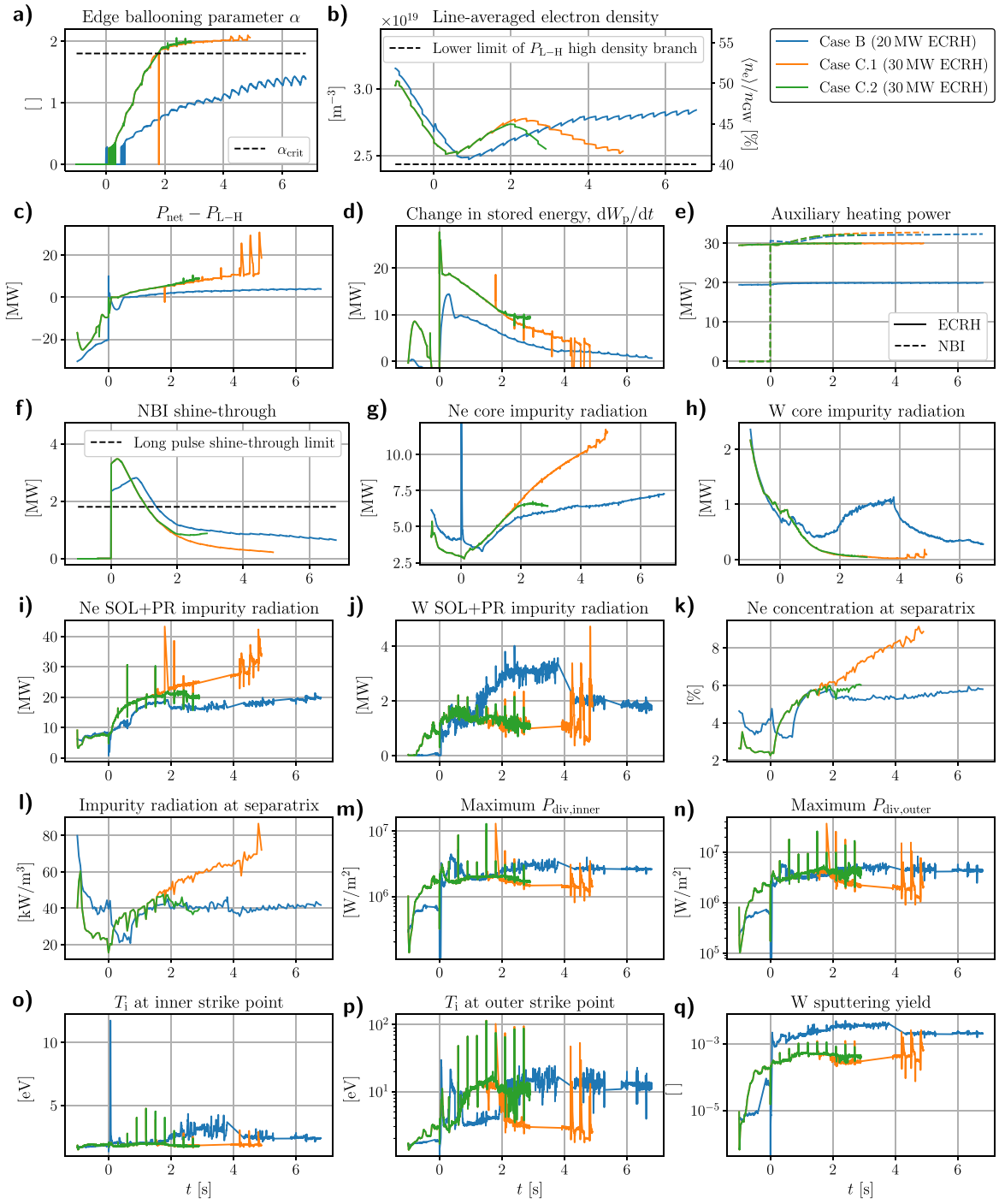

Figure 6. ITER 7.5 MA/2.65 T hydrogen plasma simulations without a helium minority. The horizontal axis in each of the plots is time [s], offset such that $t = 0$ corresponds to the time of full auxiliary power injection.

(k), respectively. The higher temperatures of the deep core also suppresses impurity radiation in these regions, with radiation being the highest in the edge (see figures 5(e) and (f)). Figure 4(i) shows the time trace of the total radiation density at the separatrix. Comparing these values to those of the other presented scenarios (figures 6(l) and 10(l)), which has higher neon seeding in order to reduce NBI shine-through, the radiation density is an order of magnitude lower for the 5 MA/1.8 T scenario.

3.2. 7.5 MA/2.65 T scenario without helium

The 7.5 MA/2.65 T hydrogen plasma scenario is planned for PFPO-2, including heating and current drive from both EC and NBI. The result of the JINTRAC simulations of cases B, C.1 and C.2, which do not include any helium, are presented in figures 6 and 7. It is apparent from figure 6(a) that case B, accessing H-mode with 20 MW of ECRH, is likely not to be able to reach type-I ELMy H-mode, with the edge

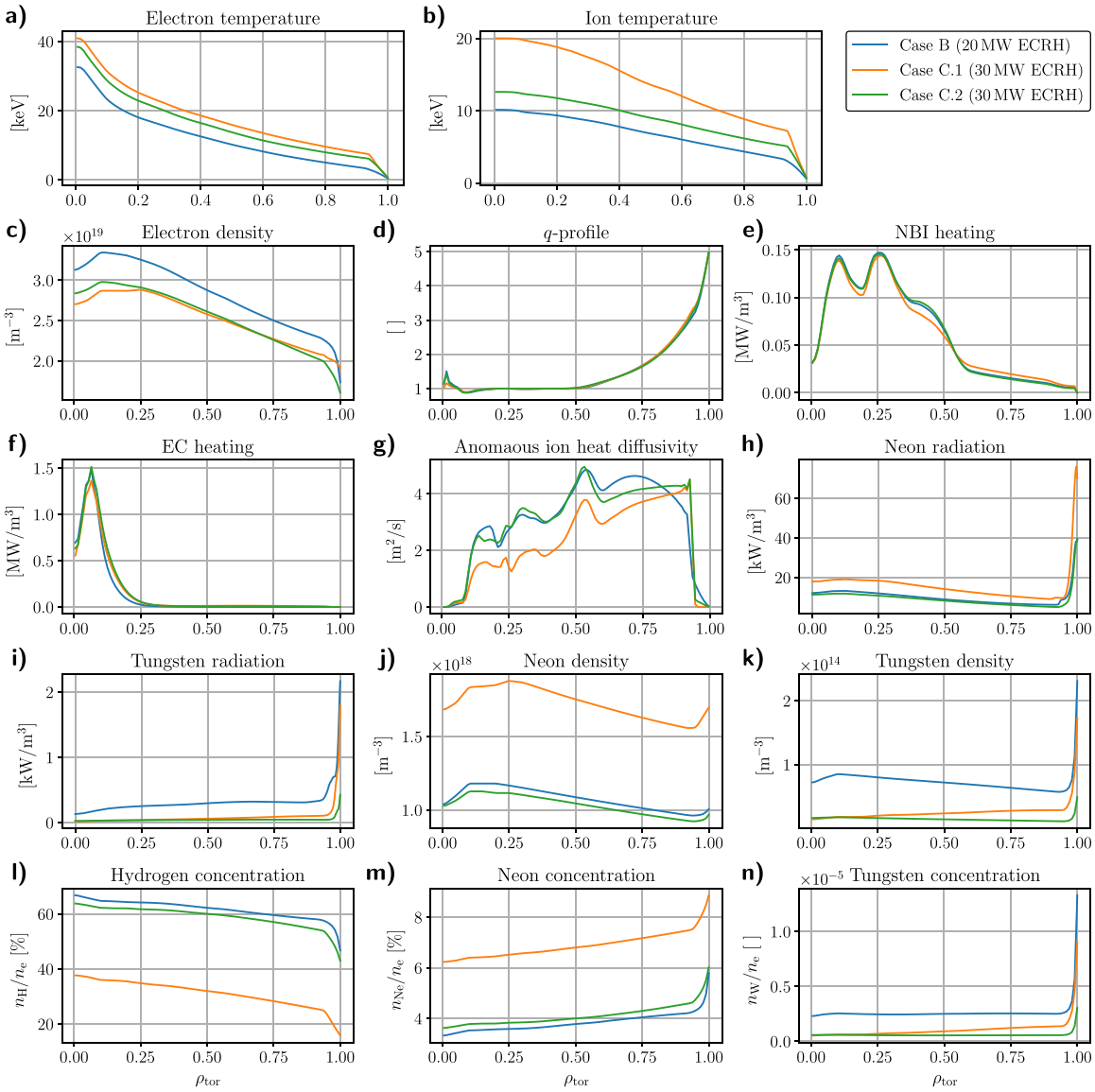

Figure 7. Core profile data for cases B, C.1 and C.2 at the end time of the simulations (case B: $t = 6.80$ s, case C.1: $t = 4.90$ s, case C.2: $t = 2.90$ s).

ballooning parameter α remaining below the estimated α_{crit}. This conclusion agrees with previous studies of the same scenario using core transport modelling with ASTRA [22]. Both cases C.1 and C.2 have α-parameters exceeding α_{crit}, indicating that 30 MW of ECRH is required for stable ELMy H-mode operation of the hydrogen plasma without a helium minority. It should be noted that the line-averaged electron density of case B (see figure 6(b)) stabilises about 14–16% above the lower limit of the high-density branch $n_{e,min}$, meaning that it is theoretically possible to reach $11\% \approx 4$ MW lower P_{L-H} when operating exactly at $\langle n_e \rangle = n_{e,min}$. According to figure 6($c$), case B stabilises at around 4 MW net power above the L-H power threshold, meaning that the margin above the threshold could in principle be doubled, which might be sufficient to operate at a stable ELMy H-mode. However, considering the narrow operation margins of case B, combined with the uncertainty of $n_{e,min}$ in ITER, access to ELMy H-mode at 20 MW ECRH cannot be taken for granted.

Case C.1 was excessively seeded with neon to reduce the NBI shine-through, with the final shine-through power around 0.2 MW (see figure 6(f)), well below the estimated long-pulse shine-through limit at 1.8 MW, and the neon core impurity radiation finishing close to 12 MW (see figure 6(g)). This should be compared to case C.2, which is the same case as C.1, but with reduced neon seeding. The NBI shine-through for this case stabilises around 0.9 MW, and the neon core impurity radiation at around 6.5 MW, meaning that there is a net gain of about 4.8 MW input power compared to case C.1. However, this relative gain is cancelled in P_{net} to some extent by differences in dW_p/dt. The net power P_{net}, which is compared against P_{L-H} in figure 6(c), is calculated as $P_{aux} + P_{ohm} - P_{rad} - \langle dW_p/dt \rangle$, where W_p is the total stored

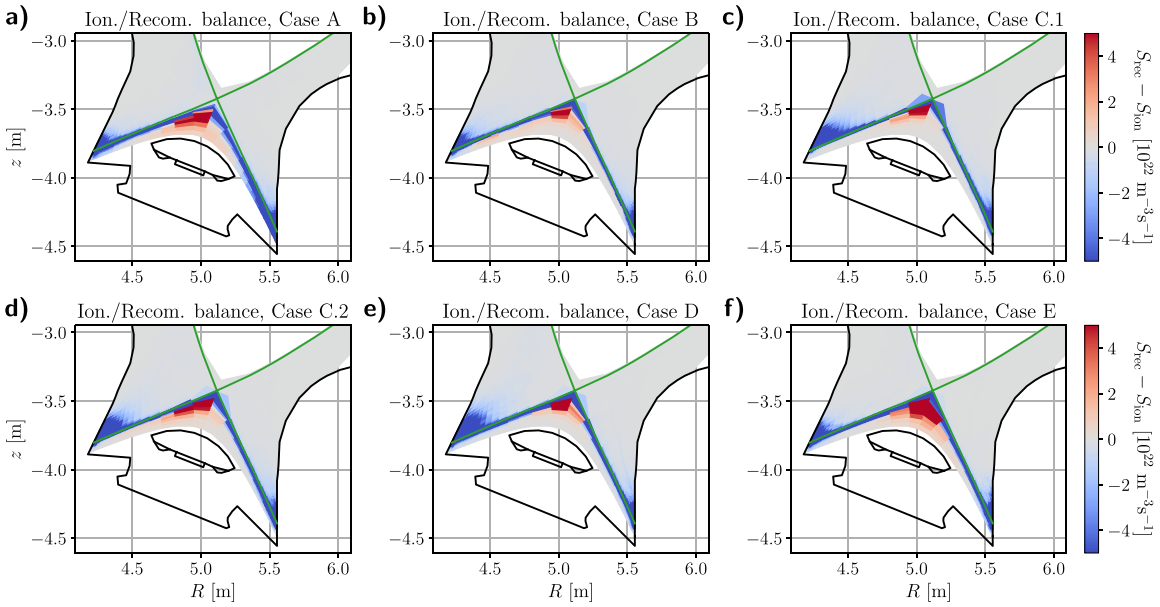

Figure 8. Difference between recombination and ionisation rates for all six cases. The colourmaps have been truncated at $\pm 5 \times 10^{22}\,\mathrm{m}^{-3}\mathrm{s}^{-1}$.

energy. Neither case C.1 nor C.2 have reached stationary conditions, which would have been indicated by $\mathrm{d}W_\mathrm{p}/\mathrm{d}t \approx 0$ in figure 6(*d*). However, the simulations have run sufficiently long to conclude that type-I ELMy H-mode is accessible in the 30 MW ECRH scenario, as α has already stabilised above α_crit, and a reduction of $\langle \mathrm{d}W_\mathrm{p}/\mathrm{d}t \rangle$ will only increase the margin above the L-H power threshold.

As mentioned in section 2.4, there is a risk of reaching regimes of full detachment if the edge region is cooled down significantly by gas puffing and impurity radiation. To verify that neither of the presented scenarios has reached full detachment, including Case C.1, which was excessively seeded by neon, the recombination rates are compared against the ionisation rates for all cases in figure 8. Full detachment would be indicated by a region around the separatrix, in particular around the x-point, where $S_\mathrm{rec} > S_\mathrm{ion}$. All of the cases have a limited domain in the private region where $S_\mathrm{rec} > S_\mathrm{ion}$. This means that the modelling indicates that the scenarios are only partially detached at most.

In figure 6(*k*), the neon concentration is calculated as a fraction of the electron density. This value stabilised around 6% for cases B and C.2, whereas it reached 9% (and increasing) towards the end of case C.1, indicating an almost pure neon plasma at the separatrix for that case (the full neon concentration profile at the end time of each simulation can be seen in figure 7(*m*)). Although neon is more efficient at sputtering tungsten from the divertor than hydrogen, case C.1 did not show higher tungsten radiation compared to cases B and C.2 (see figures 6(*h*) and (*j*)). This could be a consequence of the high neon radiation in the SOL (figure 6(*i*)), which keeps the strike point ion temperature down and reduces the overall sputtering from the divertor. Case B demonstrated relatively high strike point ion temperatures (figures 6(*o*) and (*p*)) and tungsten sputtering yield (figure 6(*q*)). However, with tungsten core impurity radiation below the MW range, the tungsten content in the plasma volume is not sufficient to substantially impact the H-mode operation. The maximum power loads on the inner and outer divertor target plates stabilise at a few MW m^{-2} (see figures 6(*m*) and (*n*)), besides a couple of discrete bursts, particularly on the outer target plates in cases C.1 and C.2. The bursts in divertor power loads are associated with particle and heat fluxes in the outer part of the plasma due to large predicted anomalous transport following sawtooth crashes.

Core profile data for cases B, C.1 and C.2 is shown in figure 7. Case C.1 has significantly higher ion temperature (figure 7(*b*)), which could be explained by the lower anomalous ion diffusivity (figure 7(*g*)). Neither of the cases show the same non-monotonicity of the electron temperature as case A. This is because the additional 10 MW ECRH is injected from a hypothetical equatorial launcher in O-mode, allowing for more on-axis electron heating. There is a non-monotonic deposition of the NBI power density, but the relatively spread out absorption in ρ_tor does not affect the shape of the electron or ion temperature profiles significantly. Again, sawtooth crashes extend to $\rho_\mathrm{tor} \approx 0.5$, as seen in figure 7(*d*). While impurity radiation profiles for cases B, C.1 and C.2 are qualitatively the same as the ones for case A, they are between 1 and 2 orders of magnitude larger (compare figures 6(*h*) and (*i*) with figures 4(*e*) and (*f*), respectively). This is due to the additional requirement for neon to reduce the NBI shine-through, which in turn sputters tungsten from the divertor more effectively than hydrogen. The hydrogen fraction is significantly lower in cases B, C.1 and C.2 compared to case A (compare figures 7(*l*) with 5(*i*)), and case C.1 in particular, where it is as low as 16%

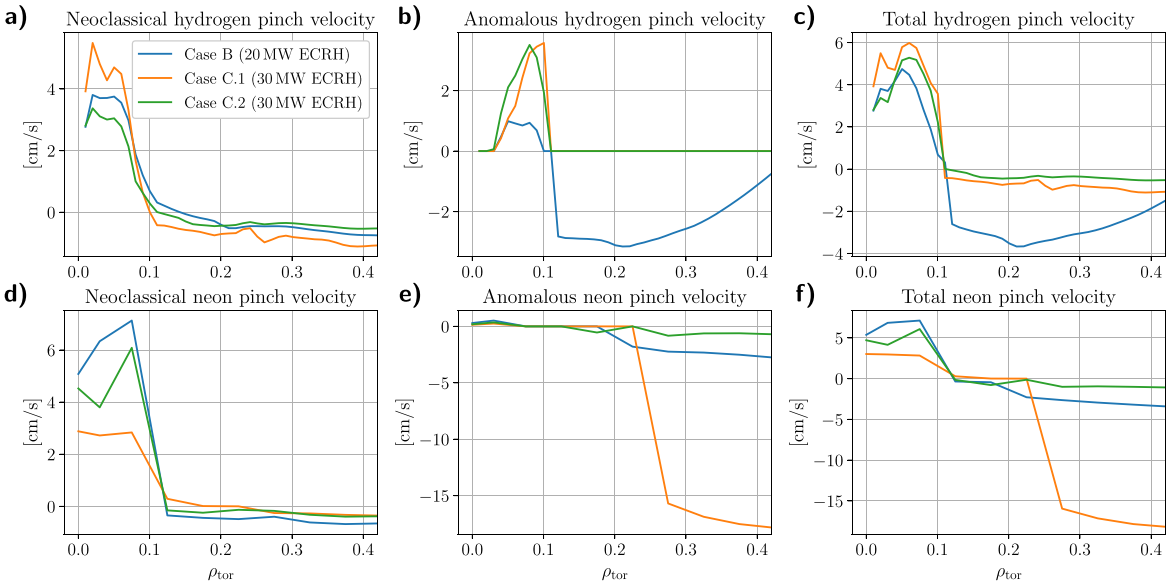

Figure 9. Neoclassical and anomalous pinch velocity components for hydrogen and neon at the end time of the simulations (case B: $t = 6.80$ s, case C.1: $t = 4.90$ s, case C.2: $t = 2.90$ s). The total pinch velocity is the sum of the neoclassical and anomalous components.

at the separatrix. This is again due to the higher neon content of these cases.

The electron temperature peaks at $\rho_{tor} \approx 0.1$ rather than on-axis, as seen in figure 7(c). This non-monotonicity cannot be attributed to the sawtooth crashes, since the peaking is well inside the $q \approx 1$ domain ($\rho_{tor} \lesssim 0.5$). Figure 9 shows the hydrogen and neon pinch velocity profiles for the three cases at the final time of the simulations, split into neoclassical and anomalous components. All cases show a positive neoclassical pinch velocity inside of $\rho_{tor} \approx 0.1$, and a weakly negative neoclassical pinch outside. The anomalous pinch is positive in the same domain, but with lower pinch velocity than the neoclassical values, and negative anomalous pinch velocities are also found at $\rho_{tor} \gtrsim 0.1$ for all cases, except for the hydrogen pinch for cases C.1 and C.2. For the total pinch velocity (figures 9(c) and (f)), all three cases show the same trend, which tends to accumulate the plasma towards $\rho_{tor} \approx 0.1$. The particle diffusivity balances this accumulation to some extent. However, it is not enough to flatten the off-axis density peak. Neon transport has a similar impact on the electron density as hydrogen, since the charge densities are comparable. The steep on-axis T_e gradient, as seen in figure 7(a), is contributing to the neoclassical pinch [39].

3.3. 7.5 MA/2.65 T scenario seeded with helium

In the two cases presented in figure 10 (cases D and E), the 7.5 MA/2.65 T hydrogen plasma has been seeded with helium for presumed lowering of the L–H power threshold, as discussed in section 2.3. This increases the net power above the threshold for improved H-mode quality. Figure 10(a) confirms that stable type-I ELMy H-mode operation is reached both for the 20 MW and the 30 MW ECRH cases. Unlike cases A, B, C.1 and C.2, the cases D and E use a combination of hydrogen gas puffing and pellet injection to fuel the plasma, as discussed in section 2.4. The pellet injection rate is adapted for reaching target averaged electron densities. The target density for the 20 MW ECRH case (case D) is set close to $n_{e,min}$, whereas the target density for the 30 MW ECRH case (case E) is between 55 and 60% above $n_{e,min}$, corresponding to $\langle n_e \rangle / n_{GW}$ between 62 and 64%, as seen in figure 10(b). The higher target density for case E is chosen to demonstrate a wider operational space with 30 MW ECRH, although it increases the L–H power threshold by up to about 40% = 12 MW.

The NBI power is gradually increased until it finally reaches its full power at $t = 0$, as demonstrated in figure 10(e). The NBI shine-through power stabilises around 1.3–1.5 MW for both cases (figure 10(f)), which is below the assumed limit of 1.8 MW for long-pulse operation. Slightly lower neon content is required for sufficient beam stopping in case E compared to case D because of the higher averaged density. This is also reflected in the lower neon core radiation of case E in figure 10(g). However, the neon radiation in the SOL and private region is similar for the two cases, stabilising around 20 MW, as seen in figure 10(i). As for the 7.5 MA/2.65 T cases with no helium (cases B, C.1 and C.2), the tungsten radiation is negligible compared to the neon radiation, as seen in figures 10(h) and (j).

The maximum power load on the divertor target plates stabilises around 2–6 MW m^{-2} (see figures 10(m) and (n)), which is well within acceptable long-pulse operational limits. However, there are frequent bursts in the power loads, in particular at the outer target during the initial stages of the H-mode. Again, the largest bursts coincide with wide sawtooth crashes, inducing significant particle and heat fluxes in the outer core plasma via bursts in anomalous diffusivity. Since the bursts are very short and drop in frequency during later stages of the H-mode confinement, they are unlikely to cause

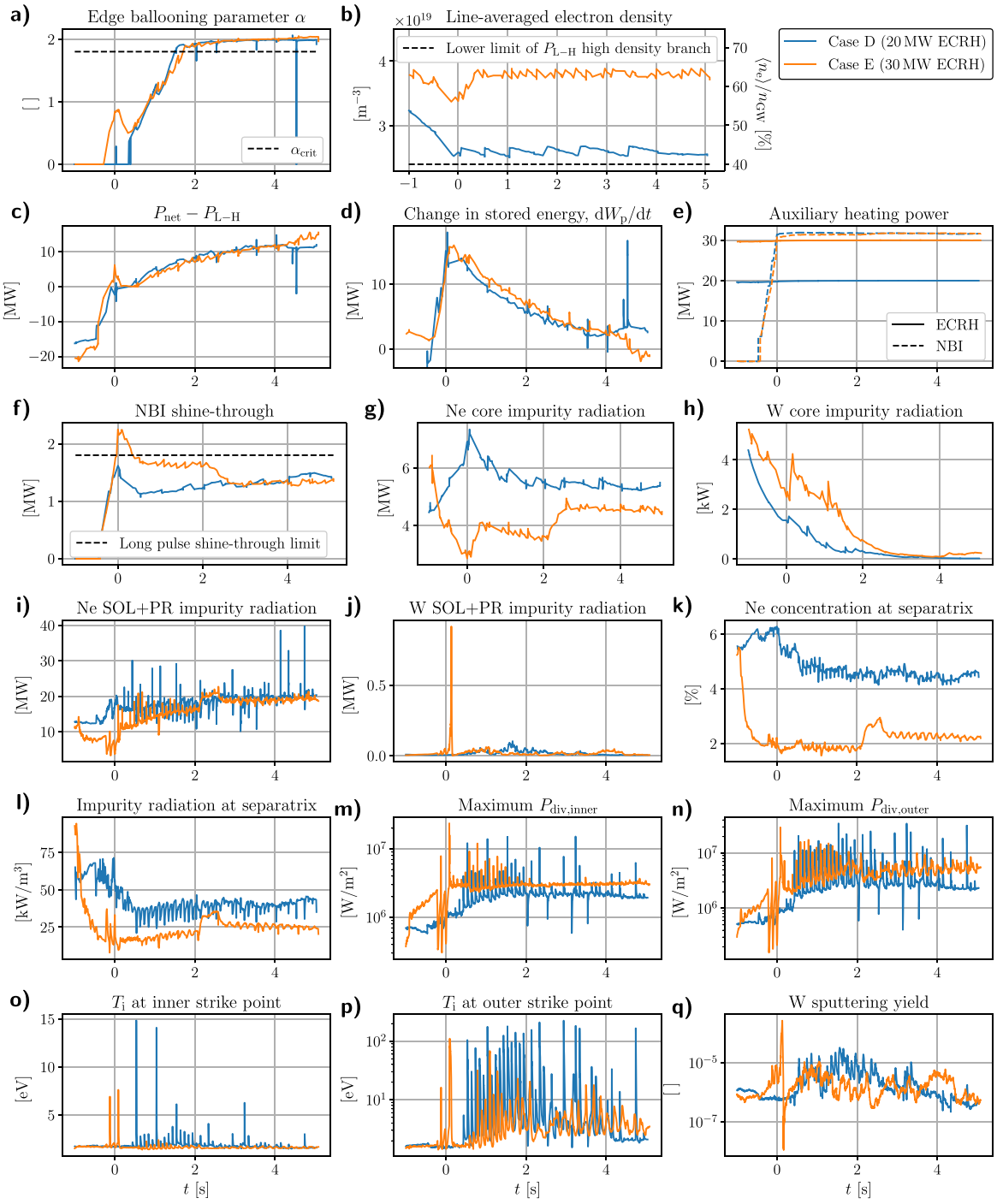

Figure 10. ITER 7.5 MA/2.65 T hydrogen plasma simulation with a helium minority. The horizontal axis in each of the plots is time [s], offset such that $t = 0$ corresponds to the time of full auxiliary power injection.

significant reduction of the divertor lifetime. The ion temperature of the strike points are also sustained at relatively low levels at the order of 1 eV, with the exception of discrete bursts, as seen in figures 10(o) and (p). This causes a very low tungsten sputtering yield of the order 10^{-6} (see figure 10(q)), which is 2–3 orders of magnitude lower than any of the other presented cases.

Similarly to case A, cases D and E show some degree of non-monotonicity of the temperature profiles (figures 11(a) and (b)), due to a combination of sawtooth crashes and off-axis heating. Cases D and E used a magnetic reconnection factor of 1.0 for the Kadomtsev model, whereas the other cases used a reconnection factor of 0.3. The main reason for the higher reconnection factor was to make a pessimistic assumption about the impact of sawteeth on the scenarios, such as higher amplitude oscillations of the plasma state and their impact on e.g. tungsten sputtering. The lower reconnection factor is more in agreement with experimental results from JET. The higher reconnection factor of Cases D and E could cause steeper pressure gradients across the $q = 1$ boundary close to $\rho_{tor} = 0.5$

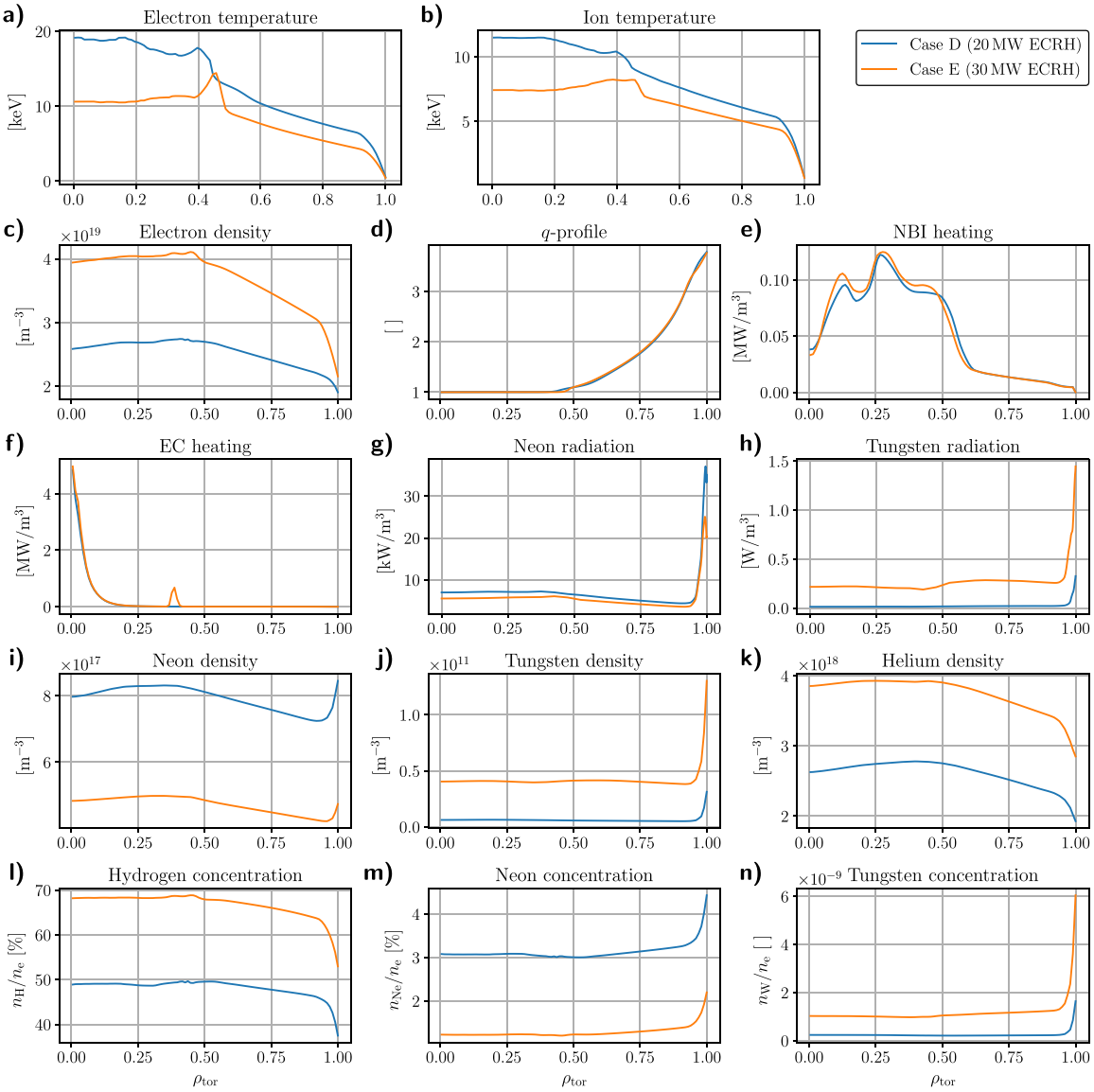

Figure 11. Core profile data for cases D and E at the end time of the simulations (case D: $t = 5.04$ s, case E: $t = 5.08$ s).

(see $q \approx 1$ domain in figure 11(*d*)). With neon gas puffing being overall lower in cases D and E compared to the corresponding cases with no helium (cases B, C.1 and C.2), both the neon density (figure 11(*i*)), concentration (figure 11(*m*)) and radiation density (figure 11(*g*)) are lower (compare against figures 7(*j*), (*m*) and (*h*), respectively). The tungsten density and radiation levels are exceptionally low for cases D and E compared to other cases, with densities of the order 10^{10} m^{-3} and radiation densities below 1 W/m^3 in most of the core plasma, which is a result from the low sputtering yield. However, with the neon concentration being of the order of a few % in the core plasma, it is enough to significantly reduce the hydrogen concentration, as seen in figure 11(*l*). Case D, which operates at lower density than case E, and consequently requires more neon for sufficient beam stopping, has a core concentration of hydrogen of less than 50%.

4. Conclusions and discussion

ITER will undergo a PFPO phase, during which stable H-mode confinement will be demonstrated and several operational systems will be commissioned. For the commissioning of ELM mitigation systems, stable operation in type-I ELMy H-mode is required. The presented paper investigates the possibility to operate the 7.5 MA/2.65 T and 5 MA/1.8 T hydrogen plasma scenarios for this purpose, using core plasma and edge/SOL/divertor integrated modelling tools. Furthermore, it is tested whether the currently planned ECRH power capacity is sufficient for stable ELMy H-mode operation or a proposed 10 MW upgrade of the EC systems is required. The L–H power threshold of the hydrogen plasma is expected to be a factor ~2 larger compared to equivalent deuterium plasma scenarios. Operation at low density and seeding the plasma with a helium

minority are both methods used to attempt to reduce the power threshold for easier H-mode access. While H-mode access and margin to the L–H transition can be estimated with core plasma modelling, a complete assessment of the viability of these scenarios in ITER requires full core/edge/SOL modelling, which is done for the study presented in this paper. Many of the strategies followed to lower the L–H transition have direct implications on the SOL and plasma–wall interaction (PWI) aspects with effects (such as full detachment or excessive W contamination of the core plasma) that can counter balance the expected effects from core plasma simulations and make, in practice, the scenarios for H-mode access and sustainment in ITER not viable. The modelling performed in this paper identifies which of such strategies will lead to realisable PFPO H-mode scenarios with core-edge-PWI factors taken into account.

The 5 MA/1.8 T scenario is planned for the early stages of PFPO, during which only electron cyclotron resonance power systems are available for auxiliary heating, whereas the 7.5 MA/2.65 T scenario is also assisted by NBI heating. Neon is seeded by gas puffing to reduce NBI shine-through and to prevent excessive power loads to the divertor. Excessive neon seeding can potentially impede access to type-I ELMy H-mode by reducing the margin of net power above the L–H power threshold via core impurity radiation. The presented modelling, which includes self-consistent treatment of neon seeding, tungsten sputtering from the divertor, impurity transport, and atomic physics, is used to investigate whether the neon seeding can be optimised for sufficient beam stopping and divertor cooling without compromising ELMy H-mode access for the different scenarios. All modelled cases start from L-mode confinement at reduced auxiliary power, eventually ramping up to full input power to demonstrate a stable L–H transition. Once a quasi-stationary H-mode flat-top has been reached, the edge ballooning parameter α is compared against the estimated threshold, α_{crit}, for triggering type-I ELMs (using a continuous ELM model in this paper).

Modelling results indicated that the 7.5 MA/2.65 T hydrogen plasma scenario might more readily access ELMy H-mode either through seeding by helium or a 10 MW upgrade of the EC systems. The success of the helium seeded scenario without the ECRH power upgrade relies on the assumptions that a) the lower limit of the high-density branch of the L–H power threshold is similar to or lower than $0.4n_{\mathrm{GW}}$, and b) a 10% helium minority reduces $P_{\mathrm{L-H}}$ by 15%. Both assumptions are based on results from JET experiments, for which it is unknown how well they extrapolate to ITER operation regimes. In particular, the lower limit of the $P_{\mathrm{L-H}}$ high-density branch has shown to vary significantly with the strike-point configuration at JET. The 10 MW ECRH upgrade allows for operation in ELMy H-mode at higher density, which has been demonstrated for the helium seeded case. This relaxes the assumption that the lower limit of the $P_{\mathrm{L-H}}$ high-density branch $n_{\mathrm{e,min}}$ is at $0.4n_{\mathrm{GW}}$, giving more confidence in robust access to H-mode based on the assumed $P_{\mathrm{L-H}}$ scaling.

The 5 MA/1.8 T hydrogen plasma scenario has a lower Greenwald density compared to the 7.5 MA/2.65 T scenario due to the lower plasma current. The scenario can consequently operate at a lower absolute density while staying above the lower limit of the $P_{\mathrm{L-H}}$ high-density branch. However, the lower available auxiliary power means that the 10 MW ECRH upgrade is still likely required to operate in a stable ELMy H-mode. With an expected L–H power threshold at around 20 MW at $\langle n_e \rangle = n_{\mathrm{e,min}} \approx 0.4n_{\mathrm{GW}}$, H-mode confinement can at best be marginally reached with 20 MW of ECRH, not allowing access to type-I ELMy H-mode operation.

Acknowledgments

JINTRAC was used under licence agreement between Euratom and CCFE, reference Ares(2014)3576010 - 28/10/2014. This work was part funded by the RCUK Energy Programme [Grant Number EP/T012250/1], EPSRC Energy Programme [Grant Number EP/W006839/1], and by ITER Task Agreement C19TD53FE implemented by Fusion for Energy under Grant GRT-869 and Contract OPE-1057. The views and opinions expressed herein do not necessarily reflect those of the ITER Organization. To obtain further information on the data and models underlying this paper please contact PublicationsManager@ukaea.uk.

ORCID iDs

E. Tholerus https://orcid.org/0000-0002-3262-1958
L. Garzotti https://orcid.org/0000-0002-3796-9814
F. Eriksson https://orcid.org/0000-0002-2740-7738
D. Farina https://orcid.org/0000-0003-0795-3632
L. Figini https://orcid.org/0000-0002-0034-4028
A. Loarte https://orcid.org/0000-0001-9592-1117
E. Militello Asp https://orcid.org/0000-0001-8183-8734
S.D. Pinches https://orcid.org/0000-0003-0132-945X
P. Strand https://orcid.org/0000-0002-8899-2598

References

[1] Campbell D.J. *et al* 2024 ITER Research Plan within the Staged Approach (Level III–Final version) *ITER Technical Report* ITR-18-005 ITER Organization (available at: www.iter.org/technical-reports/)
[2] Loarte A. *et al* 2024 Initial evaluations in support of the new ITER baseline and Research Plan *ITER Technical Report* ITR-24-004 ITER Organization (availabele at: www.iter.org/technical-reports/)
[3] Coenen J.W. *et al* 2015 *J. Nucl. Mater.* **463** 78
[4] Budaev V.P. *et al* 2015 *J. Nucl. Mater.* **463** 237
[5] Li M. and You J.H. 2016 *Nucl. Mater. Energy* **9** 598
[6] Gunn J.P. *et al* 2017 *Nucl. Fusion* **57** 046025
[7] Loarte A. *et al* 2014 *Nucl. Fusion* **54** 033007
[8] Kirk A. *et al* 2013 *Plasma Phys. Control. Fusion* **55** 124003
[9] Lang P.T. *et al* 2004 *Nucl. Fusion* **44** 665
[10] Baylor L.R. *et al* 2013 *Phys. Rev. Lett.* **110** 245001
[11] Degeling A., Martin Y., Lister J., Villard L., Dokouka V., Lukash V. and Khayrutdinov R. 2003 *Plasma Phys. Control. Fusion* **45** 1637

[12] Lang P.T. *et al* 2004 *Plasma Phys. Control. Fusion* **46** L31
[13] Romanelli M. *et al* 2014 *Plasma Fusion Res.* **9** 3403023
[14] Koechl F. *et al* 2017 *Nucl. Fusion* **57** 086023
[15] Leoni C. *et al* 2024 *50th EPS Conf on Plasma Physics (Salamanca, Spain, 8–12 July 2024) 48A P1.038* (available at: https://iris.uniroma1.it/retrieve/f3a23fe8-3067-4483-9c00-e773a60d48b9/Leoni_Scrape-Off%20Layer_2024.pdf)
[16] Ho A., Citrin J., Auriemma F., Bourdelle C., Casson F., Kim H., Manas P., Szepesi G., Weisen H. and Contributors J.E.T. 2019 *Nucl. Fusion* **59** 056007
[17] Staebler G., Bourdelle C., Citrin J. and Waltz R. 2024 *Nucl. Fusion* **64** 103001
[18] Kalupin D., Wiesen S., Andrew Y., Tokar M., Parail V., Reiser D., Corrigan G., Korotkov A. and Spence2 J. JET EFDA contributors 2008 *Nucl. Fusion* **48** 085006
[19] Kumpulainen H., Groth M., Corrigan G., Harting D., Koechl F., Järvinen A., Lomanowski B., Meigs A., Sertoli M. and Contributors J.E.T. 2020 *Nucl. Mater. Energy* **25** 100866
[20] Groth M. *et al* 2023 *Nucl. Mater. Energy* **34** 101372
[21] Chankin A., Corrigan G., Maggi C. and Contributors J. 2019 *Plasma Phys Control. Fusion* **61** 075010
[22] Polevoi A., Campbell D., Chuyanov V., Houlberg W., Ivanov A., Kukushkin A., Lamalle P., Loarte A., Mukhovatov V. and Oikawa T. 2013 *Nucl. Fusion* **53** 123026
[23] Kim S.H. *et al* 2017 *Nucl. Fusion* **57** 086021
[24] Loarte A. *et al* 2021 *Nucl. Fusion* **61** 076012
[25] Polevoi A.R. *et al* 2023 *Nucl. Fusion* **63** 076003
[26] Angioni C., Citrin J., Loarte A., Polevoi A., Kim S., Fable E. and Tardini G. 2023 *Nucl. Fusion* **63** 126035
[27] Pereverenzev G. and Yushmanov P. 2002 ASTRA Automated System for TRansport Analysis IPP-Report IPP 5/98 Institute of Plasma Physics Garching, Germany (available at: https://pure.mpg.de/pubman/item/item_2138238_1/component/file_2138237/IPP-5-98.pdf/)
[28] Cenacchi G. and Taroni A. 1988 JETTO: A free boundary plasma transport code JET-IR(88)03 (available at: https://inis.iaea.org/records/7h4y6-32977)
[29] Simonini R., Corrigan G., Radford G., Spence J. and Taroni A. 1994 *Contrib. Plasma Phys.* **34** 368
[30] Wiesen S. 2006 EDGE2D/EIRENE code interface report ITC project report 2005/6 (available at: www.eirene.de/e2deir_report_30jun06.pdf/)
[31] Reiter D., May C., Coster D. and Schneider R. 1995 *J. Nucl. Mater.* **220–222** 987
[32] Lerche E. *et al* 2012 *Plasma Phys. Control. Fusion* **54** 074008
[33] Schneider M., Artaud J.-F., Bonoli P., Kazakov Y., Lamalle P., Lerche E., van Ester D. and Wright J. 2017 *EPJ Web Conf.* **157** 03046
[34] Kazakov Ye O. *et al* 2021 *Phys. Plasmas* **28** 020501
[35] Oikawa T., Shimada M., Polevoi A., Naito O., Bonoli P., Hayashi N., Kessel C. and Ozeki T. 2006 Study on Current Drive Capability of Lower Hybrid Waves and Neutral Beam in an ITER Steady State Scenario *Proc. 21st Int. Conf. on Fusion Energy (Chengdu, China, 16–21 October 2006) IT/P1-4* (availabel at: https://citeseerx.ist.psu.edu/document?repid = rep1&type = pdf&doi = 56918bd9b5c870d3f31e6e2ac66cabef2e8ae0da/)
[36] Polevoi A., Ivanov A., Medvedev S., Huijsmans G., Kim S., Loarte A., Fable E. and Kuyanov A. 2020 *Nucl. Fusion* **60** 096024
[37] Farina D. 2007 *Fusion Sci. Technol.* **52** 154
[38] Challis C.D., Cordey J.G., Hamnén H., Stubberfield P.M., Christiansen J.P., Lazzaro E., Muir D.G., Stork D. and Thompson E. 1989 *Nucl. Fusion* **29** 563
[39] Houlberg W.A., Shaing K.C., Hirshman S.P. and Zarnstorff M.C. 1997 *Phys. Plasmas* **4** 3230
[40] Martin Y.R. and Takizuka T. the ITPA CDBM H-mode Threshold Database Working Group 2008 *J. Phys. Conf. Ser.* **123** 012033
[41] Righi E. *et al* 1999 *Nucl. Fusion* **39** 309
[42] Maggi C.F. *et al* 2014 *Nucl. Fusion* **54** 023007
[43] Delabie E. *et al* 2015 *42nd EPS Conf. on Plasma Physics (Lisbon, Portugal, 22–26 June 2015) 39E O3.113* (available at: https://info.fusion.ciemat.es/OCS/EPS2015PAP/pdf/O3.113.pdf/)
[44] Hillesheim J.C. *et al* 2017 *44th EPS Conf. on Plasma Physics (Belfast, United Kingdom, 26–30 June 2017) 41F P5.162* (available at: https://info.fusion.ciemat.es/OCS/EPS2017PAP/pdf/P5.162.pdf/)
[45] Solano E.R. *et al* 2021 *Nucl. Fusion* **61** 124001
[46] Pégourié B., Waller V., Nehme H., Garzotti L. and Géraud A. 2007 *Nucl. Fusion* **47** 44
[47] Singh M.J., Boilson D., Polevoi A.R., Oikawa T. and Mitteau R. 2017 *New J. Phys.* **19** 055004
[48] Lauro-Taroni L., Alper B., Giannella R., Lawson K., Marcus F., Mattioli M., Smeulders P. and von Hellermann M. 1994 *21st EPS Conf. on Controlled Fusion and Plasma Physics (Montpellier, France, 27 June–1 July 1994), 18B 102* (available at: http://libero.ipp.mpg.de/libero/PDF/EPS_21_Vol1_1994.pdf/)
[49] Summers H.P., Dickson W.J., O'Mulane M.G., Badnell N.R., Whiteford A.D., Brooks D.H., Lang J., Loch S.D. and Griffin D.C. 2006 *Plasma Phys. Control. Fusion* **48** 263
[50] Henderson S.S., Bluteau M., Foster A., Giunta A., O'Mullane M.G., Pütterich T. and Summers H.P. 2017 *Plasma Phys. Control. Fusion* **59** 055010
[51] Strand P.I., Bateman G., Eriksson A., Houlberg W.A., Kritz A.H., Nordman H. and Weiland J. 2004 *31st EPS Conf. on Plasma Physics (London, United Kingdom, 28 June–2 July 2004) 28G P5.187* (available at: https://info.fusion.ciemat.es/OCS/EPS2004/pdf/P5_187.pdf)
[52] Casati A. 2009 A quasi-linear gyrokinetic transport model for tokamak plasmas *PhD Thesis* Université de Provence, France (available at: https://inis.iaea.org/records/fc315-1d981/files/42013883.pdf)
[53] Bourdelle C., Garbet X., Imbeaux F., Casati A., Dubuit N., Guirlet R. and Parisot T. 2007 *Phys. Plasmas* **14** 112501
[54] Erba M., Aniel T., Basiuk V., Becoulet A. and Litaudon X. 1998 *Nucl. Fusion* **38** 1013
[55] Tholerus E. *et al* 2024 *Nucl. Fusion* **64** 106030
[56] Casper T., Gribov Y., Kavin A., Lukash V., Khayrutdinov R. and Fujeda H. Kessel C (for the ITER Organization and ITER Domestic Agencies) 2014 *Nucl. Fusion* **54** 013005
[57] Crontiger J.A. et al 1997 CORSICA: a comprehensive simulation of toroidal magnetic-fusion devices Tech. Rep. UCRL-ID-126284 Lawrence Livermore National Laboratory. NTIS #PB2005-102154 (available at: https://digital.library.unt.edu/ark:/67531/metadc691657/m2/1/high_res_d/522508.pdf)
[58] Khayrutdinov R.R. and Lukash V.E. 1993 *J. Comput. Phys.* **109** 193
[59] Kadomtsev B.B. 1975 *Sov. J. Plasma Phys.* **1** 389
[60] Parail V. *et al* 2009 *Nucl. Fusion* **49** 075030